Cross-Filament Stochastic Acceleration of Electrons in Kilojoule Picosecond Laser Interactions with Near-Critical-Density Plasmas

X. F. Shen,[1,*] A. Pukhov,[1,†] O. N. Rosmej,[2,3] and N. E. Andreev[4,5]

[1] *Institut für Theoretische Physik I, Heinrich-Heine-Universität Düsseldorf, Düsseldorf 40225, Germany*
[2] *GSI Helmholtzzentrum für Schwerionenforschung GmbH, Planckstrasse 1, Darmstadt 64291, Germany*
[3] *Helmholtz Forschungsakademie Hessen für FAIR (HFHF), Campus Frankfurt am Main, Max-von-Laue-Straße 12, Frankfurt am Main 60438, Germany*
[4] *Joint Institute for High Temperatures, RAS, Izhorskaya Street 13, Building 2, Moscow 125412, Russia*
[5] *Moscow Institute of Physics and Technology (State University), Institutskiy Pereulok 9, Dolgoprudny Moscow Region 141700, Russia*

(Received 3 February 2022; revised 19 June 2022; accepted 16 November 2022; published 29 December 2022)

Understanding the interaction of a kilojoule picosecond laser pulse with long-scale-length preplasma or homogeneous near-critical-density (NCD) plasma is crucial for guiding experiments at national short-pulse laser facilities. Using full three-dimensional particle-in-cell simulations, we demonstrate that in this regime, cross-filament stochastic acceleration is an important mechanism that contributes to the production of superponderomotive high-flux electron beams. Since the laser power significantly exceeds the threshold of the relativistic self-focusing, multiple filaments are generated and can propagate independently over a long distance. Electrons jump across the filaments during the acceleration and their motion becomes stochastic. We find that the effective temperature of electrons increases with the total interaction time following a scaling like $T_{\rm eff} \propto \tau_i^{0.65}$. By irradiating a submillimeter-thick NCD target, the space charge of electrons with energy above 2.5 MeV reaches tens of microcoulombs. Such high-flux electrons with superponderomotive energies significantly facilitate applications in high-energy-density science, nuclear science, secondary sources, and diagnostic techniques.

DOI: 10.1103/PhysRevApplied.18.064091

I. INTRODUCTION

The advent of kilojoule laser facilities, such as the National Ignition Facility Advanced Radiographic Capability (NIF-ARC) [1], the Laser MegaJoule PETawatt Aquitaine Laser (LMJ-PETAL) [2], and the Laser for Fast Ignition Experiment (LFEX) [3], expands the frontier of laser-plasma interaction (LPI). It has attracted great attention [4–18] due to its broad applications in high-energy-density (HED) science [13,19], probing [8,20] and driving [21,22] inertial confinement fusion (ICF), production of high-flux electron beams [5,6,16] and secondary sources (e.g., ions, neutrons, and x rays or γ rays) [9,17,18], laboratory astrophysics [23], nuclear science [24], etc. These lasers are limited to deliver picosecond pulses with large focal spots of tens of micrometers due to both technological and infrastructure constraints [17]. The interaction physics of such pulses with plasmas is quite different from the usually discussed subpicosecond pulses with diffraction-limited small focal spots (typically, < 10 μm) [25–32]. On the one hand, the long interaction time brings us to the mesoscale between kinetic and fluid regimes; on the other, the large focal spot results in quasi-one-dimensional plasma expansion in laser-solid target interactions. However, in underdense plasmas, it may trigger filamentation instability [33–36], since the laser power is several orders of magnitude higher than the threshold of relativistic self-focusing [37,38]. The enhancement of scalings of electron [6,12,14,15,17] and proton acceleration [9,17,18] has been observed in experiments and simulations but the debate about the acceleration mechanisms still remains controversial.

Previous studies of such laser pulses have focused on the interaction with overdense plasmas and the effects of the long pulse duration. Theoretical investigations have mainly relied on one- or two-dimensional (2D) particle-in-cell (PIC) simulations, since three-dimensional (3D) simulations demand large computational resources. However, to thoroughly understand the underlying physics and quantitatively explain the experimental results, it is essential to conduct 3D simulation studies. On the other hand, recent experimental and numerical researches have demonstrated that in the interactions of femtosecond or

*shenx@hhu.de
†pukhov@tp1.uni-duesseldorf.de

subpicosecond laser pulses with small focal spots with near-critical-density (NCD) plasmas, the maximum energy and flux of both electrons and ions can be much higher than those obtained with solid targets [31,39–44]. This is because a long plasma channel is formed due to the self-focusing and coalescence of adjacent filaments, in which abundant electrons are accelerated predominantly by direct laser acceleration (DLA) [45–48]. However, when a laser pulse with a large focal spot is used, the distances between neighboring filaments may be much larger than the skin depth, so they do not influence each other and the coalescence cannot proceed further [35]. Therefore, many channels survive for a long time. This self-focusing process can only be properly described by 3D simulations, the reason for which has been explained in Ref. [35]. Nevertheless, how it affects the LPI on the multipicosecond time scale, especially for electron acceleration, is still unclear.

In this paper, we investigate the long-time interaction of realistic picosecond laser pulses with large focal spots with submillimeter NCD plasmas via full-scale 3D PIC simulations. We find that most energetic electrons are no longer confined in an individual channel. They are first accelerated by DLA in a channel and then they may jump across into adjacent channels. This triggers the stochastic motion of electrons. As a result, electrons can be further heated up to superponderomotive energies. The effective electron temperature increases with the interaction time (defined by the laser pulse duration and depletion in an extended NCD plasma) as $T_{\text{eff}} \propto \tau_i^{0.65}$.

II. SIMULATION PARAMETERS AND MAIN RESULTS

We conduct 3D PIC simulations with the Virtual Laser Plasma Lab (VLPL) code by considering realistic laser and plasma parameters [49]. A y-polarized laser with an intensity of 4.74×10^{19} W/cm^2 and a wavelength of $\lambda = 1$ μm is incident on a fully ionized homogeneous plasma with an electron density of $n_e = 0.65 n_c$ and length 400λ. Here, $n_c = m_e \omega_0^2 / 4\pi e^2$ is the critical density, where ω_0, m_e, and e are the laser frequency, electron mass, and charge, respectively. The temporal and spatial profiles are Gaussian distributions. The pulse length is $\tau_L = 0.7$ ps [full width at half maximum (FWHM)] and the whole interaction time reaches over 3 ps. The focal spot is $d_L = 50\lambda$ (FWHM), leading to a power of 1.5 PW and an energy of 1 kJ. The ion composition is $n_{C^{6+}} : n_{H^+} : n_{O^{8+}} = 3 : 4 : 2$ [31,39,50]. The simulation box is $425\lambda \times 250\lambda \times 250\lambda$. The first 10λ and last 15λ spaces in the x direction are vacuum. The longitudinal resolution is $h_x = 0.1\lambda$. In transverse dimensions, within the focal spot (i.e., $|y, z| < 42\lambda$), a finer resolution of $h_y = h_z = 0.5\lambda$ is used, while outside this region, the cell size increases exponentially by a factor of 1.05 to save computational resources. A numerical Cherenkov-free rhombi-in-plane (RIP) Maxwell solver is used [51]. We use four macroparticles per cell for electrons and one for ions of each type. The numerical convergence is confirmed by comparing the physical quantities of interest at different resolutions.

The laser power is more than 4 orders of magnitude higher than the power threshold of relativistic self-focusing [37,38] of $P_{cr} = 17(\omega_0/\omega_p)^2 \approx 26$ GW. Therefore, the laser pulse breaks up into many small filaments when it enters the plasma. Each carries the critical power and undergoes the self-focusing process. Figure 1 illustrates the temporal evolution of the magnetic fields $|B_z|$ [Figs. 1(a)–1(c)] and the electron density [Figs. 1(b)–1(d)] at $t = -0.033$ ps [Figs. 1(a) and 1(b)] and 0.367 ps [Figs. 1(c) and 1(d)]. One can clearly see evidence of the multifilaments in the B_z field and the corresponding multichannels in the density distribution. The channels are not evacuated completely and the residual electron density is about $0.2 n_c$. During the interaction, the maximum laser intensity reaches 2×10^{20} W/cm^2 due to the self-focusing.

In Fig. 2, we show the temporal evolution of the transverse modes by analyzing the B_z field, where it is evident that over a long time, the dominant mode is around $0.2k_0$, especially when the laser peak enters the plasma ($t = 0$). This means that the distance between neighboring filaments is usually much larger than the skin depth $d_s = c/\omega_p$. Therefore, the magnetic fields are shielded by the surrounding plasma and the coalescence induced by magnetic attraction cannot occur further naturally [35,52]. The channels can remain almost straight and well separated up to $t = 0.367$ ps. After that, induced by hosinglike instability [53,54] and transverse expansion of ions [35], the distances between neighboring channels can become smaller and some of them merge into several larger ones [Figs. 1(c) and 1(d)], corresponding to the longer modes in Fig. 2(c). The laser pulse is completely absorbed at $x = 375\lambda$ and $t = 1.767$ ps (about 3 ps after the start of LPI), while the self-generated quasistatic magnetic field can last for an even longer time. Note that since the average distance between two neighboring filaments is about 10 times larger than our transverse resolution, the fundamental physical phenomena should be similar, with even higher resolution.

In our regime, most of the laser energy is absorbed by the plasma. This is a key advantage compared to laser-solid target interaction [55–57]. The conversion efficiency from laser to particles reaches 84%. At $t = 2.1$ ps, the energy carried by electrons is about 770 J and the rest is mainly absorbed by ions, in which protons, carbon ions, and oxygen ions carry 16.7 J, 27.1 J, and 24.1 J, respectively. In VLPL, we register all electrons that leave from the simulation-box boundaries. The space charge of forward-moving electrons with energies above 2.5 MeV reaches 38 μC (approximately 2.4×10^{14}), which is more than one order of magnitude higher than that reported in Ref. [18], where solid targets and 450-J laser energy have been used.

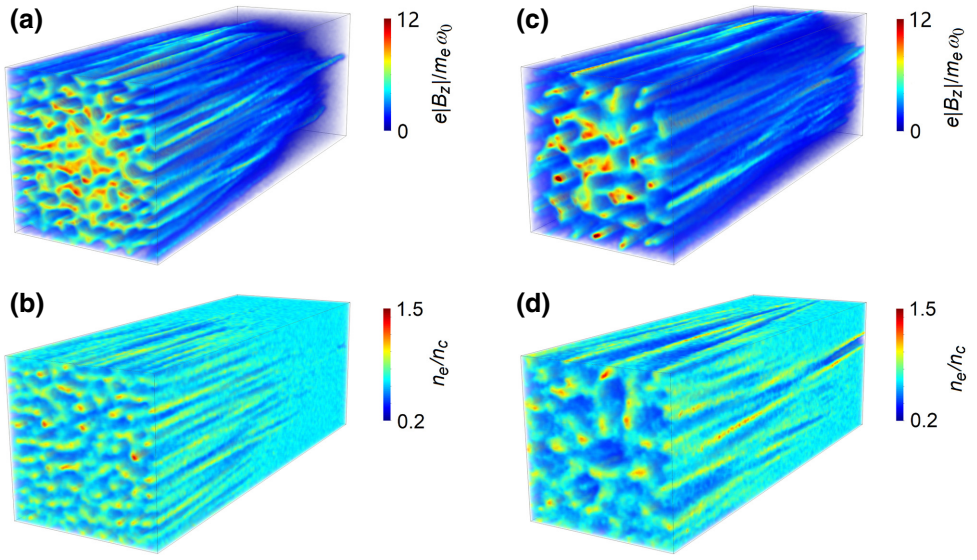

FIG. 1. The 3D PIC simulation results of a long NCD plasma irradiated by a kilojoule picosecond laser pulse. The magnetic field $|B_z|$ [(a),(c)] and electron density [(b),(d)] are presented at $t = -0.033$ ps [(a),(b)] and 0.367 ps [(c),(d)], respectively, showing that strong filamentation occurs when a large-focal-spot laser is used. Here, $t = 0$ corresponds to the time when the laser peak enters the plasma. Only part of the simulation box (within $\pm 30\lambda$ and a length of 90λ) is shown.

In Fig. 3, we show the energy distribution [Fig. 3(a)] and divergence [Fig. 3(b)] of electrons, in which, for electrons registered at the side boundaries, we only consider those high-energy ones with $\gamma > 16$. This leads to a total space charge of electrons of about 7.6 μC, while the space charge of electrons confined inside 15° (almost all of them are registered at the rear boundary) is only about 0.3 μC. A distinctive feature is that the peak brightness appears at around 30°, instead of in the laser direction, the difference between which is about a factor of 2. This feature can be used to distinguish the cross-filament stochastic acceleration (CFSA) from other acceleration mechanisms [6,11,14,45,58] in experiment. The effective temperatures $T_{\rm eff}$ around angles of 0° and 15° are 10.8 MeV and 8.6 MeV, respectively, much larger than the ponderomotive scaling [25] $T_{\rm pond} = (\sqrt{1 + a_0^2/2} - 1)m_e c^2 \approx$ 1.6 MeV. At 45°, the temperature is much lower, at about 3.8 MeV. Moreover, the relatively low forward flux can be partly attributed to the Alfvén current limit [59] $J_A = m_e c^3 \beta\gamma/e = 17\beta\gamma$ kA. Taking the beam length about 1 ps and $\gamma = 20$ ($\simeq T_{\rm eff}$), this gives 0.34 μC.

The effective temperature of electrons inside the box at $t = 2.1$ ps is about 2.2 MeV, as shown in Fig. 4(a), while for protons and carbon ions, the corresponding effective temperatures are about 800 keV and 4.4 MeV [i.e., 367 keV/μ; see the red and blue lines in Fig. 4(b)]. There are 5×10^{14} protons with energy > 10 keV and 10^{13} protons with energy above the threshold (i.e., 1.64 MeV) of the ^{7}Li$(p,n)^7$Be reaction [60]. Since the characteristic energies of protons and carbon ions (per nucleon) are lower than that of electrons, subsequently, the electron energy will be further transferred to ions via thermal expansion over a much longer time, leading to even more abundant

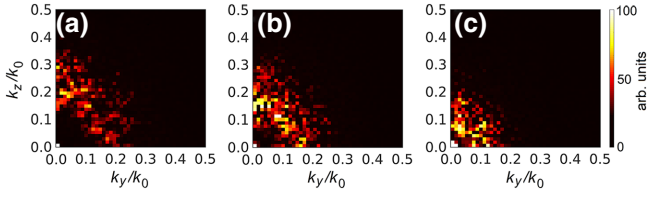

FIG. 2. The temporal evolution of the wave-number spectra of the B_z field observed at $x = 50\lambda$: (a) $t = -0.233$ ps; (b) $t = -0.033$ ps; (c) $t = -0.367$ ps. The color scale corresponds to the relative spectral intensity.

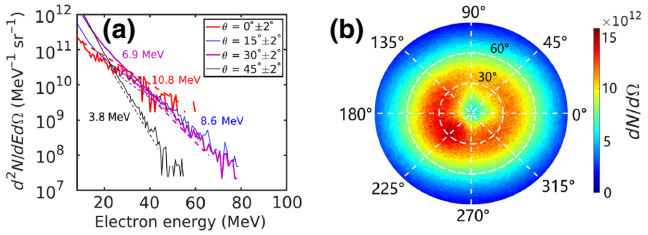

FIG. 3. (a) The energy spectra per steradian $d^2N/dEd\Omega$ of electrons that leave the simulation box up to $t = 2.767$ ps around $\theta = 0°$ (red), 15° (blue), 30° (magenta), and 45° (black), where $d\Omega = \sin\theta d\theta d\phi$, $\theta = \arctan(\sqrt{p_y^2 + p_z^2})/p_x$ and $\phi = \arctan(p_z/p_y)$. (b) The angular distribution of the high-energy electrons.

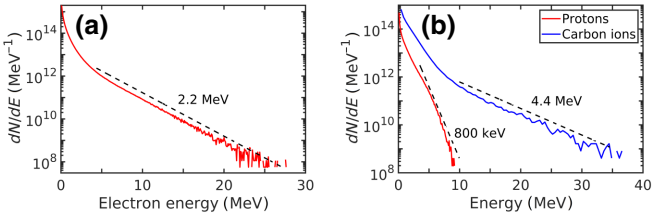

FIG. 4. (a) The energy spectrum of electrons that stay inside the simulation box at $t = 2.1$ ps. (b) The energy spectra of protons (red) and carbon ions (blue) that stay inside the initial plasma boundary (i.e., $10\lambda < x < 410\lambda$) at $t = 2.1$ ps.

energetic ions. This result may find applications in the production of high-flux neutrons by replacing some of the plasma components with nuclear materials [61–64].

III. ELECTRON-ACCELERATION DYNAMICS

A. Stochastic acceleration

To understand the underlying physics, we perform 3D simulations with a particle tracer. Hereinafter, the laser intensity is fixed at 4.74×10^{19} W/cm^2. A laser pulse with a smaller focal spot of $d_L = 35.3\lambda$ and a shorter pulse duration of $\tau_L = 500$ fs is used to reduce the computational cost. The plasma density is $0.75n_c$, to deplete the pulse in a shorter distance. In Fig. 5(a), we present the 2D cut of the electron density distribution at $t = 0.117$ ps, where many filaments are formed. The solid lines, color coded with respect to the γ factor, depict the trajectories of several representative electrons. One can see that these electrons jump across multichannels during their acceleration, different from that in DLA, where resonant electrons are trapped in a single channel and undergo betatron oscillation [31,45]. When the electrons jump from one channel to the neighboring channels, their motions become stochastic. This is because in different channels, the phase of the laser field, determined by the residual electron density and the channel direction, is different [65]. Here, the origin of the stochastic motion is different from that in the well-known regime, where it is induced by two counterpropagating pulses [58].

Figure 5(b) shows the CFSA process of a representative electron, where the electron trajectory (the colored line) is plotted on top of the transverse field in a comoving window with a width of $\Delta_y = \pm 30\lambda$. The black line illustrates the time evolution of the electron γ. One can see that the electron experiences lots of random kicks (corresponding to oscillations of γ) as it jumps across the filaments and that the value of γ is slowly increasing.

To evaluate the stochasticity of the system, we calculate the Lyapunov exponent λ_{Ly} [66,67]:

$$\lambda_{Ly} = \frac{2\pi}{\omega_0 \Delta t} \ln \frac{\sum |\mathbf{P}(\mathbf{P_0} + \delta\mathbf{P}) - \mathbf{P}(\mathbf{P_0})|}{\sum |\delta\mathbf{P}|}, \qquad (1)$$

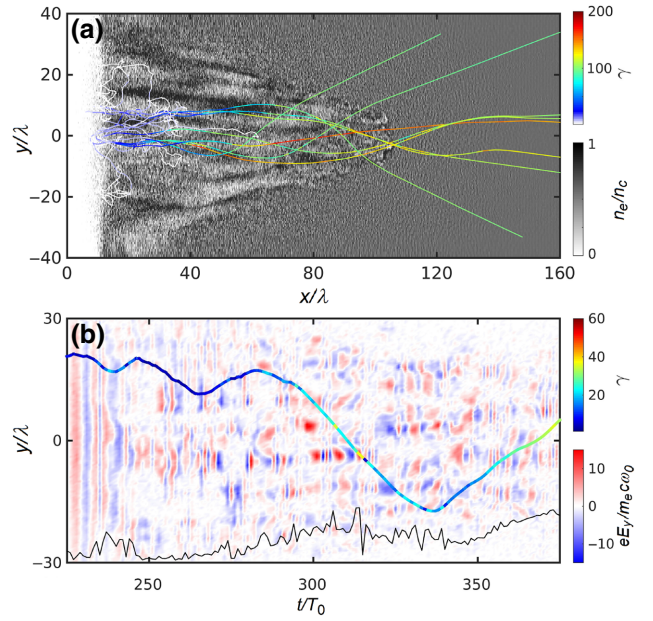

FIG. 5. (a) The particle trajectories and density distribution, showing that electrons jump across several filaments during the acceleration. (b) The witnessed E_y field for a representative electron that experiences CFSA. The black line shows the evolution of the γ factor. In (a) and (b), the trajectories of electrons are shown by the lines color coded with their corresponding γ factor.

where $\mathbf{P}(\mathbf{P_0})$ and $\mathbf{P}(\mathbf{P_0} + \delta\mathbf{P})$ are the electron momentum without and with perturbation, respectively, $\delta\mathbf{P}$ is initial momentum perturbation, and Δt is the time that has elapsed after the perturbation added in simulation. Here, we add $\delta\mathbf{P} = \delta P_x = 0.01 m_e c$ at $t = -0.2$ ps. For negative λ_{Ly}, the system is stable to small perturbations. However, if λ_{Ly} is positive, the system is chaotic. The calculation of Eq. (1) is shown in Fig. 6(a), where the black line represents the Lyapunov exponent λ_{Ly} averaged over 300 particles the initial positions of which are randomly distributed near the front of the plasma and the red line shows the λ_{Ly} for a representative single particle. In Figs. 6(b) and 6(c), we present the trajectory and momenta space of

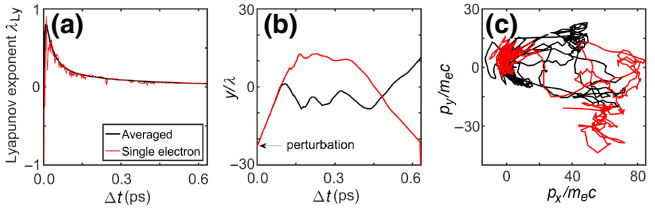

FIG. 6. The stochasticity of the electron acceleration. (a) The time evolution of the λ_{Ly}, demonstrating that the electron motion is stochastic. The black line shows the average λ_{Ly}, while the red line is from a single electron. (b),(c) The (b) trajectories and (c) momentum space of this electron with (red) and without (black) perturbations are shown.

this electron, respectively, where the black line represents the case without perturbation and the red with perturbation. It is evident that λ_{Ly} is always positive and that a tiny perturbation results in exponentially diverging trajectories [Fig. 6(b)] and momentum space [Fig. 6(c)]. Therefore, we conclude that the electron motion is stochastic and that the electrons experience CFSA.

B. Scaling

Another important feature of the stochastic acceleration is that the effective temperature increases with the interaction time [68]. A similar trend has also been observed in recent experiments, where large-focal-spot laser pulses with different τ_L (determining τ_i) have been used [17]. In Ref. [68], a simple analytical model has been proposed to explain this feature, where single-electron motion in a planar laser pulse is investigated by considering some friction. The increase of the longitudinal momentum after averaging over the laser cycle is [68]

$$\left\langle \frac{dp_x}{dt} \right\rangle \approx \frac{\nu_\perp a_0^2}{2[1+(\gamma\nu_\perp/\omega_0)^2]} - \nu_\parallel \langle p_x \rangle , \tag{2}$$

where $\nu_\parallel$ and $\nu_\perp$ denote the friction constants along the x and y directions. Since it is only friction in the y direction that has a strong effect on the acceleration, we can assume that $\nu_\parallel = 0$ for simplicity. For those forward-moving electrons with $p_x \gg p_y$, we can rewrite the above equation as

$$\left\langle \frac{d\gamma}{dt} \right\rangle \approx \frac{\nu_\perp a_0^2}{2m_e c} \frac{1}{1+(\gamma\nu_\perp/\omega_0)^2}. \tag{3}$$

Then, one can easily see that the electron energy increases with the time. In the case of $1 \gg (\gamma\nu_\perp/\omega_0)^2$ (small friction), we have $\langle\gamma\rangle \propto t$, while in the case of $1 \ll (\gamma\nu_\perp/\omega_0)^2$ (large friction), we have $\langle\gamma\rangle \propto t^{1/3}$. This is broadly consistent with the numerical results shown in Ref. [68], where the authors have found that the effective temperature scales with the interaction time t^q with $q \approx 0.5$–1.0.

In our scheme, when electrons jump across filaments, they experience transverse friction coming from the self-generated electromagnetic fields surrounding the filaments. Therefore, the above simple model can be used to describe the main physical process in our scheme. However, considering the evolution of the fields over multiple picoseconds and also the relativistic effects, it is impossible to quantitatively give an exact derivation of the exponent q. Therefore, we have to resort to PIC simulations.

To obtain the electron energy scaling of our scheme, we perform further 3D PIC simulations by varying τ_L. The final energy spectrum of the electrons from each simulation is shown in Fig. 7(a). The scaling can be given as [see Fig. 7(b)]

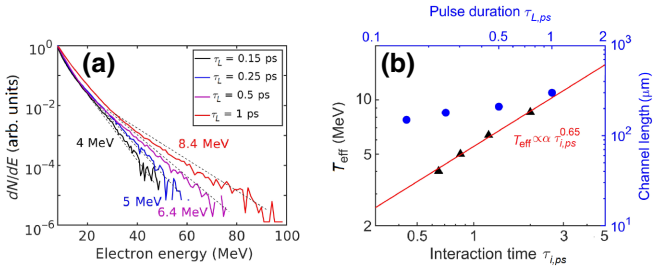

FIG. 7. (a) Electron energy spectra from different pulse durations. (b) T_{eff} versus $\tau_{i,ps}$, where the red line represents the best fit and the blue circles show the channel length of each case. Here, the energy spectra are integrated over the solid angles $n_e = 0.75n_c$ and $I_0 = 4.74 \times 10^{19}$ W/cm^2.

$$T_{\mathrm{eff}} \sim \alpha (I/I_{18})^{0.5} (\tau_{i,ps})^{0.65}, \tag{4}$$

where the coefficient $\alpha \approx 0.8$ and $\tau_{i,ps}$, normalized to 1 ps, is the interaction time. The exponent of 0.65 is within the range predicted by the simple analytical model [68]. Here, we determine $\tau_i = \tau_L + l_{ch}/c$, where l_{ch} is the channel length observed in the simulations, as specified by the blue circles in Fig. 7(b).

C. Triggering condition

In CFSA, the long-surviving multiple filaments are crucial. The conditions for CFSA as the predominant acceleration mechanism are given by

$$d_L \frac{\omega_{rp}}{c} \sim 15, \tag{5}$$

$$2t_i \geq \tau_L \gg 2\pi/k_f c, \tag{6}$$

where $\omega_{rp} = \omega_p/\sqrt{\gamma}$ is the relativistically corrected plasma frequency and $t_i = 2^{1/4}\sqrt{m_i/Za_0m_e}r_L/c$ is the time for ions to move across the laser spot size. Equation (5) describes the threshold of the filamentation instability [69,70] and Eq. (6) determines that many filaments can survive when the laser peak arrives [55], while electrons have time to jump across multiple filaments. For the parameters considered here, we estimate that $d_L \sim 10\lambda$ and $t_i \approx 4$ ps. Considering the status of kilojoule picosecond laser facilities, CFSA should always be a predominant acceleration mechanism in LPI with long NCD plasmas unless $\tau_L \gg t_i$.

According to Eq. (5), suppression of the filamentation instability requires $d_L \sim 12.3\lambda$, where we assume $\gamma = 20$ and $n_e = 0.75n_c$ based on the parameters used in Fig. 5. As a demonstration, we show 3D PIC simulations with laser focal spot sizes larger ($d_L = 23.6\lambda$) and smaller ($d_L = 11.8\lambda$) than the threshold in Figs. 8(a) and 8(b), respectively. One can clearly see that when the focal spot size is smaller than the threshold, a single channel is formed

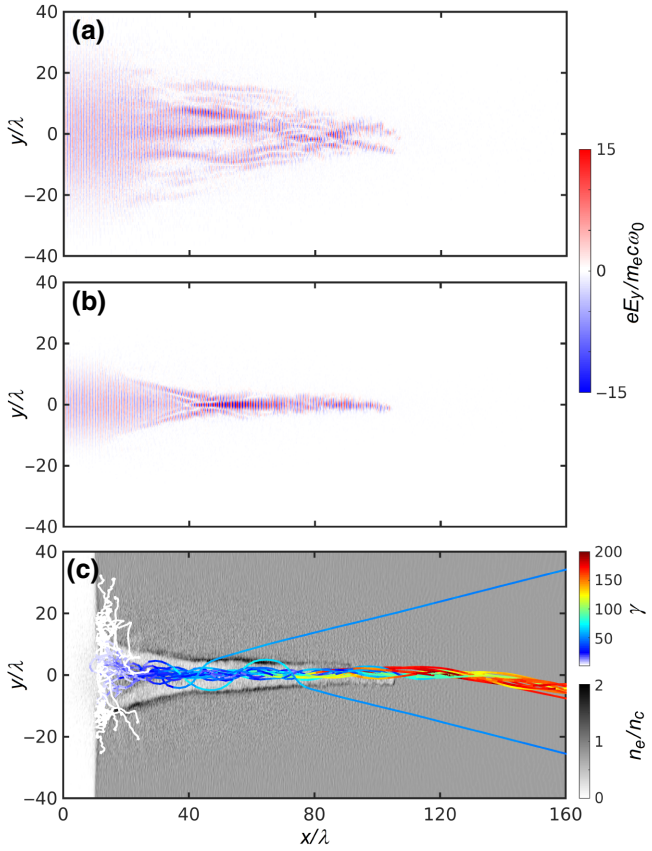

FIG. 8. (a),(b) The distributions of the laser electric field E_y at $t = 0.117$ ps for the cases with laser focal spot $d_L = 23.6\lambda$ and 11.8λ, respectively. (c) The electron trajectories (colored lines) and the density distribution for the case with $d_L = 11.8\lambda$, showing that with a small focal spot, most of the energetic electrons are confined in a single channel and accelerated via the DLA mechanism. In (c), the solid lines show the trajectories of the selected electrons with their relativistic γ factor color coded.

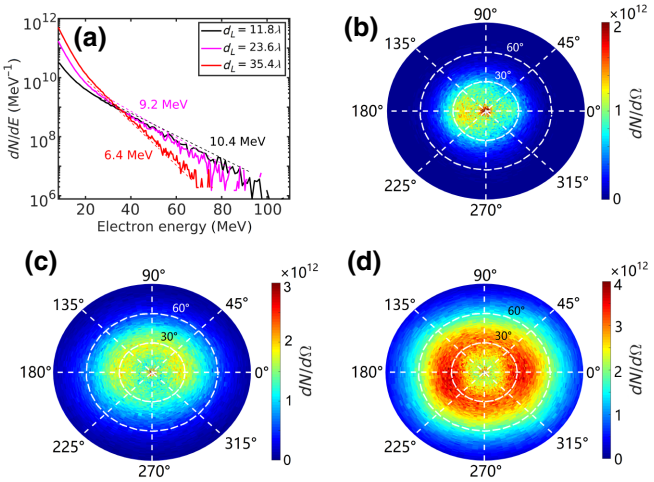

FIG. 9. (a) The electron energy spectra registered at the boundaries for the cases with focal spot size $d_L = 11.8\lambda$ (black), 23.6λ (magenta), and 35.4λ (red). (b)–(d) The corresponding angular distributions of the high-energy electrons. Note that here the energy spectra are integrated over the solid angles, $n_e = 0.75n_c$, $I_0 = 4.74 \times 10^{19}$ W/cm^2, and $\tau_L = 500$ fs.

[Figs. 8(b) and 8(c)], while when it is larger, multiple filaments appear. In Fig. 8(c), we show the trajectories of electrons and the electron density distribution for the single-channel case, where it is evident that most of the energetic electrons are confined inside the channel and undergo betatron oscillation. This is a typical phenomena of DLA.

IV. SUMMARY AND DISCUSSION

As discussed in Sec. III, with the increase of the laser focal spot size, the electron acceleration may transit from DLA to CFSA due to the arising of the filamentation instability. To show the difference in the features of the electron beams obtained from these two mechanisms, in Fig. 9(a) the energy spectra of electrons from the cases with focal spot size $d_L = 11.8\lambda$, 23.6λ, and 35.4λ are depicted by the solid black, magenta, and red lines, respectively, while the angular distributions are correspondingly shown in Figs. 9(b)–9(d).

One can see that with a narrow pulse where DLA predominates, the obtained electron beam has a higher electron temperature and maximum electron energy compared to the cases from wider pulses where CFSA predominates. This is because in DLA, electrons can stay in the acceleration phase for a longer time. Moreover, as shown in Fig. 9(b), the electron beam from DLA is collimated in the forward direction, while in CFSA [see Figs. 9(c) and 9(d)], the peak brightness deviates from the forward direction due to the random scattering. This feature can be used in experiment to distinguish CFSA from DLA.

We note that the electron flux from CFSA is much higher than that obtained from DLA. For the case with $d_L = 35.4\lambda$, the number of electrons with energy larger than 2.5 MeV reaches 8.77×10^{13} (14 μC, registered at the boundaries), which is about 16.5 times higher than that with $d_L = 11.8\lambda$, though the laser energy is only about 9 times higher. This demonstrates that CFSA is more suitable for producing high-flux electrons compared to DLA or other known mechanisms, since in DLA, only a small part of the electrons can reach the resonant condition to be accelerated to high energies [45]. Moreover, the divergence in our scheme is comparable to or even smaller than that observed in electron-induced fast ignition [22,71,72], where the electron divergence half angle is always greater than 30° and possibly exceeds $50° - 60°$ [22]. To guide the electron transport, a cone target can be used just like that in fast ignition. On the other hand, neutron sources are usually isotropic [73] and therefore the divergence of the

electrons or protons is not that important, especially for the bulk-target regime [74].

Therefore, our work could significantly facilitate applications in HED science, particle and radiation sources, fusion energy, nuclear science, etc., where the electron flux is the key parameter, rather than the temperature or maximum energy. For example, toward the application of electron-induced fast-ignition fusion [22,71], the required electron temperature is about 1–3 MeV, to ensure that electrons can reach the dense central core and be stopped, but the required flux is extremely high (i.e., approximately 4×10^{16} electrons within 10–20 ps) [22]. Though this flux is higher than our present results, by considering appropriate laser parameters [71], it might be possible to approach the requirements via CFSA, especially due to the high conversion efficiency in our scheme. In applications of high-flux laser-based neutron sources [60,73,74] or proton-induced fast-ignition fusion [21], only moderate ion energies are required, while the ion flux needs to be huge. In the $^7\mathrm{Li}(p,n)^7\mathrm{Be}$ reaction, the proton energy of the peak of the cross section is only several megaelectronvolts [60]. To produce such proton beams, the required electron temperature should not be high, several megaelectronvolts being sufficient [56,75,76].

Furthermore, high-flux electrons can also be used to produce high-flux x rays via bremsstrahlung [77,78] or betatron radiation [32]. This is important for developing x-ray-based diagnostic techniques to probe the implosion dynamics in ICF and shock waves in related HED science, where high flux is a crucial parameter to overcome the self-emission of the plasma and achieve good statistics [79]. On the other hand, the generation of high-flux superponderomotive electrons is essential for optimizing target-normal-sheath-acceleration (TNSA) proton sources, which have become a powerful tool for probing and characterizing HED plasmas in recent years [20,80].

Though our discussion is focused on the electron acceleration in long homogeneous NCD plasmas, it should also be applicable to interactions of kilojoule picosecond lasers with solid targets where a long-scale-length preplasma appears. The preplasma can be induced by either the prepulse [17,18] or the long-time interaction [5]. The formation of multifilaments in long-scale-length preplasmas has been observed [34,35,50]. Therefore, we deduce that CFSA can also contribute to the generation of superponderomotive electrons in interactions of kilojoule picosecond lasers with solid targets [15]. Moreover, we note that due to the long-time evolution of plasma and field structures, other mechanisms may also contribute to the electron acceleration [6,11,14,45] but CFSA may manifest itself in the angular distribution of electrons [see Fig. 3(b)] if it becomes the predominant mechanism.

In conclusion, we perform a systematic study on interactions of realistic kilojoule picosecond lasers with submillimeter NCD plasmas. We demonstrate that due to multifilament formation, copious electrons jump across multichannels and obtain superponderomotive energies from the stochastic acceleration. We find that the electron temperature grows with the pulse duration. Our work provides an attractive approach for producing high-flux electron beams and secondary sources, including ions [21], neutrons [60], x rays [77,78], etc., which can be further used in important applications from diagnostic techniques to fusion energy.

ACKNOWLEDGMENTS

This work is supported by the Deutsche Forschungsgemeinschaft (DFG) (project PU 213/9). We gratefully acknowledge the Gauss Centre for Supercomputing e.V. [81] for funding this project (qed20) by providing computing time through the John von Neumann Institute for Computing (NIC) on the GCS Supercomputer JUWELS at Jülich Supercomputing Centre (JSC). The research of N.E.A. was supported by the Ministry of Science and Higher Education of the Russian Federation (Agreement with Joint Institute for High Temperatures RAS No 075-15- 2020-785 dated September 23, 2020). X.F.S. gratefully acknowledges support by the Alexander von Humboldt Foundation, as well as helpful discussions with L. Reichwein at the Heinrich-Heine-Universität Düsseldorf.

[1] J. K. Crane *et al.*, Progress on converting a NIF quad to eight, petawatt beams for advanced radiography, J. Phys. Conf. Ser **244**, 032003 (2010).

[2] D. Batani *et al.*, Development of the PETawatt Aquitaine Laser system and new perspectives in physics, Phys. Scr. **2014**, 014016 (2014).

[3] N. Miyanaga, H. Azechi, K. A. Tanaka, T. Kanabe, T. Jitsuno, J. Kawanaka, Y. Fujimoto, R. Kodama, H. Shiraga, K. Knodo, K. Tsubakimoto, H. Habara, J. Lu, G. Xu, N. Morio, S. Matsuo, E. Miyaji, Y. Kawakami, Y. Izawa, and K. Mima, 10-kJ PW laser for the FIREX-I program, J. Phys. IV France **133**, 81 (2006).

[4] G. Li, R. Yan, C. Ren, T.-L. Wang, J. Tonge, and W. B. Mori, Laser Channeling in Millimeter-Scale Underdense Plasmas of Fast-Ignition Targets, Phys. Rev. Lett. **100**, 125002 (2008).

[5] A. J. Kemp and L. Divol, Interaction Physics of Multipicosecond Petawatt Laser Pulses with Overdense Plasma, Phys. Rev. Lett. **109**, 195005 (2012).

[6] A. Sorokovikova, A. V. Arefiev, C. McGuffey, B. Qiao, A. P. L. Robinson, M. S. Wei, H. S. McLean, and F. N. Beg, Generation of Superponderomotive Electrons in Multipicosecond Interactions of Kilojoule Laser Beams with Solid-Density Plasmas, Phys. Rev. Lett. **116**, 155001 (2016).

[7] J. Ferri, X. Davoine, S. Y. Kalmykov, and A. Lifschitz, Electron acceleration and generation of high-brilliance x-ray radiation in kilojoule, subpicosecond laser-plasma interactions, Phys. Rev. Accel. Beams **19**, 101301 (2016).

[8] H. Chen *et al.*, High-energy (>70 keV) x-ray conversion efficiency measurement on the ARC laser at the National Ignition Facility, Phys. Plasmas **24**, 033112 (2017).
[9] A. Yogo *et al.*, Boosting laser-ion acceleration with multi-picosecond pulses, Sci. Rep. **7**, 42451 (2017).
[10] J. Kim, A. J. Kemp, S. C. Wilks, D. H. Kalantar, S. Kerr, D. Mariscal, F. N. Beg, C. McGuffey, and T. Ma, Computational modeling of proton acceleration with multi-picosecond and high energy, kilojoule, lasers, Phys. Plasmas **25**, 083109 (2018).
[11] N. Iwata, S. Kojima, Y. Sentoku, M. Hata, and K. Mima, Plasma density limits for hole boring by intense laser pulses, Nat. Commun. **9**, 623 (2018); N. Iwata, Y. Sentoku, T. Sano and K. Mima, Electron acceleration in dense plasmas heated by a picosecond relativistic laser, Nucl. Fusion **59**, 086035 (2019).
[12] D. Mariscal *et al.*, First demonstration of ARC-accelerated proton beams at the National Ignition Facility, Phys. Plasmas **26**, 043110 (2019).
[13] K. Matsuo *et al.*, Petapascal Pressure Driven by Fast Isochoric Heating with a Multipicosecond Intense Laser Pulse, Phys. Rev. Lett. **124**, 035001 (2020).
[14] A. J. Kemp and S. C. Wilks, Direct electron acceleration in multi-kilojoule, multi-picosecond laser pulses, Phys. Plasmas **27**, 103106 (2020).
[15] G. J. Williams *et al.*, Production of relativistic electrons at subrelativistic laser intensities, Phys. Rev. E **103**, 031201(R) (2020); G. J. Williams, A. Link, M. Sherlock, D. A. Alessi, M. Bowers, B. P. Golick, M. Hamamoto, M. R. Hermann, D. Kalantar, K. N. LaFortune, *et al.*, Order-of-magnitude increase in laser-target coupling at near-relativistic intensities using compound parabolic concentrators, Phys. Rev. E **103**, L031201 (2021).
[16] A. E. Hussein, A. V. Arefiev, T. Batson, H. Chen, R. S. Craxton, A. S. Davies, D. H. Froula, Z. Gong, D. Haberberger, Y. Ma, P. M. Nilson, W. Theobald, T Wang, K. Weichman, G. J. Williams, and L. Willingale, Towards the optimisation of direct laser acceleration, New J. Phys. **23**, 023031 (2021).
[17] R. A. Simpson *et al.*, Scaling of laser-driven electron and proton acceleration as a function of laser pulse duration, energy, and intensity in the multi-picosecond regime, Phys. Plasmas **28**, 013108 (2021).
[18] D. Raffestin, L. Lecherbourg, I. Lantuéjoul, B. Vauzour, P. E. Masson-Laborde, X. Davoine, N. Blanchot, J. L. Dubois, X. Vaisseau, E. d'Humieres, L. Gremillet, A. Duval, Ch. Reverdin, B. Rosse, G. Boutoux, J. E. Ducret, Ch. Rousseaux, V. Tikhonchuk, and D. Batani, Enhanced ion acceleration using the high-energy petawatt PETAL laser, Matter Radiat. Extremes **6**, 056901 (2021).
[19] R. P. Drake, *Introduction to High-Energy-Density Physics* (Springer International Publishing, Berlin, 2018).
[20] R. A. Simpson *et al.*, Demonstration of TNSA proton radiography on the National Ignition Facility Advanced Radiographic Capability (NIF-ARC) laser, Plasma Phys. Control. Fusion **63**, 124006 (2021).
[21] M. Roth, T. E. Cowan, M. H. Key, S. P. Hatchett, C. Brown, W. Fountain, J. Johnson, D. M. Pennington, R. A. Snavely, S. C. Wilks, K. Yasuike, H. Ruhl, F. Pegoraro, S. V. Bulanov, E. M. Campbell, M. D. Perry, and H. Powell, Fast Ignition by Intense Laser-Accelerated Proton Beams, Phys. Rev. Lett. **86**, 436 (2001).
[22] A. P. L. Robinson, D. J. Strozzi, J. R. Davies, L. Gremillet, J. J. Honrubia, T. Johzaki, R. J. Kingham, M. Sherlock, and A. A. Solodov, Theory of fast electron transport for fast ignition, Nucl. Fusion **54**, 054003 (2014).
[23] H. Chen, F. Fiuza, A. Link, A. Hazi, M. Hill, D. Hoarty, S. James, S. Kerr, D. D. Meyerhofer, J. Myatt, J. Park, Y. Sentoku, and G. J. Williams, Scaling the Yield of Laser-Driven Electron-Positron Jets to Laboratory Astrophysical Applications, Phys. Rev. Lett. **114**, 215001 (2015).
[24] R. Mizutania, Y. Abea, Y. Arikawa, J. Nishibataa, A. Yogoa, S. R. Mirfayzia, H. Nishimuraa, K. Mimaa, S. Fujiokaa, M. Nakai, H. Shiraga, and R. Kodama, The avalanche image intensifier panel for fast neutron radiography by using laser-driven neutron sources, High Energy Density Phys. **36**, 100833 (2020).
[25] S. C. Wilks, W. L. Kruer, M. Tabak, and A. B. Langdon, Absorption of Ultra-Intense Laser Pulses, Phys. Rev. Lett. **69**, 1383 (1992).
[26] P. Gibbon and E. Förster, Short-pulse laser-plasma interactions, Plasma Phys. Control. Fusion **38**, 769 (1996).
[27] M. Zepf, E. L. Clark, F. N. Beg, R. J. Clarke, A. E. Dangor, A. Gopal, K. Krushelnick, P. A. Norreys, M. Tatarakis, U. Wagner, and M. S. Wei, Proton Acceleration from High-Intensity Laser Interactions with Thin Foil Targets, Phys. Rev. Lett. **90**, 064801 (2003).
[28] M. S. Wei, S. P. D. Mangles, Z. Najmudin, B. Walton, A. Gopal, M. Tatarakis, A. E. Dangor, E. L. Clark, R. G. Evans, S. Fritzler, R. J. Clarke, C. Hernandez-Gomez, D. Neely, W. Mori, M. Tzoufras, and K. Krushelnick, Ion Acceleration by Collisionless Shocks in High-Intensity-Laser Underdense-Plasma Interaction, Phys. Rev. Lett. **93**, 155003 (2004).
[29] A. P. L. Robinson, R. M. G. M. Trines, J. Polz, and M. Kaluza, Absorption of circularly polarized laser pulses in near-critical plasmas, Plasma Phys. Control. Fusion **53**, 065019 (2011).
[30] X. F. Shen, A. Pukhov, and B. Qiao, Monoenergetic High-Energy Ion Source via Femtosecond Laser Interacting with a Microtape, Phys. Rev. X **11**, 041002 (2021).
[31] O. N. Rosmej, M. Gyrdymov, M. M. Günther, S. Zähter, V. S. Popov, N. G. Borisenko, and N. E. Andreev, High-current laser-driven beams of relativistic electrons for high energy density research, Plasma Phys. Control. Fusion, **62**, 115024 (2020); O. N. Rosmej, X. F. Shen, A. Pukhov, L. Antonelli, F. Barbato, M. Gyrdymov, M. M. Günther, S. Zähter, V. S. Popov, N. G. Borisenko, and N. E. Andreev, Bright betatron radiation from direct-laser-accelerated electrons at moderate relativistic laser intensity, Matter Radiat. Extremes **6**, 048401 (2021).
[32] X. F. Shen, A. Pukhov, M. M. Günther, and O. N. Rosmej, Bright betatron x-rays generation from picosecond laser interactions with long-scale near critical density plasmas, Appl. Phys. Lett. **118**, 134102 (2021).
[33] A. Pukhov and J. Meyer-ter-Vehn, Relativistic Magnetic Self-Channeling of Light in Near-Critical Plasma: Three-Dimensional Particle-in-Cell Simulation, Phys. Rev. Lett **76**, 3975 (1996).

[34] K. A. Tanaka, M. M. Allen, A. Pukhov, R. Kodama, H. Fujita, Y. Kato, T. Kawasaki, Y. Kitagawa, K. Mima, N. Morio, H. Shiraga, M. Iwata, T. Miyakoshi, and T. Yamanaka, Evidence of relativistic laser beam filamentation in back-reflected images, Phys. Rev. E **62**, 2672 (2000).

[35] A. Pukhov, Strong field interaction of laser radiation, Rep. Prog. Phys. **66**, 47 (2003).

[36] A. Macchi, A. Bigongiari, F. Ceccherini, F. Cornolti, T. V. Liseikina, M. Borghesi, S. Kar, and L. Romagnani, Ion dynamics and coherent structure formation following laser pulse self-channeling, Plasma Phys. Control. Fusion **49**, B71 (2007).

[37] C. E. Max, J. Arons, and A. B. Langdon, Self-Modulation and Self-Focusing of Electromagnetic Waves in Plasmas, Phys. Rev. Lett. **33**, 209 (1974).

[38] A. B. Borisov, A. V. Borovskiy, V. V. Korobkin, A. M. Prokhorov, O. B. Shiryaev, X. M. Shi, T. S. Luk, A. McPherson, J. C. Solem, K. Boyer, and C. K. Rhodes, Observation of Relativistic and Charge-Displacement Self-Channeling of Intense Subpicosecond Ultraviolet (248 nm) Radiation in Plasmas, Phys. Rev. Lett. **68**, 2309 (1992).

[39] O. N. Rosmej, N. E. Andreev, S. Zaehter, N. Zahn, P. Christ, B. Borm, T. Radon, A. Sokolov, L. P. Pugachev, D. Khaghani, F. Horst, N. G. Borisenko, G. Sklizkov, and V. G. Pimenov, Interaction of relativistically intense laser pulses with long-scale near critical plasmas for optimization of laser based sources of MeV electrons and gamma-rays, New J. Phys. **21**, 043044 (2019).

[40] J. H. Bin, W. J. Ma, H. Y. Wang, M. J. V. Streeter, C. Kreuzer, D. Kiefer, M. Yeung, S. Cousens, P. S. Foster, B. Dromey, X. Q. Yan, R. Ramis, J. Meyer-ter-Vehn, M. Zepf, and J. Schreiber, Ion Acceleration Using Relativistic Pulse Shaping in Near-Critical-Density Plasmas, Phys. Rev. Lett. **115**, 064801 (2015).

[41] M. G. Lobok, A. V. Brantov, D. A. Gozhev, and V. Yu Bychenkov, Optimization of electron acceleration by short laser pulses from low-density targets, Plasma Phys. Control. Fusion **60**, 084010 (2018).

[42] L. Willingale, A. V. Arefiev, G. J. Williams, H. Chen, F. Dollar, A. U. Hazi, A. Maksimchuk, M. J-E. Manuel, E. Marley, W. Nazarov, T. Z. Zhao, and C. Zulick, The unexpected role of evolving longitudinal electric fields in generating energetic electrons in relativistically transparent plasmas, New J. Phys. **20**, 093024 (2018).

[43] W. J. Ma *et al.*, Laser Acceleration of Highly Energetic Carbon Ions Using a Double-Layer Target Composed of Slightly Underdense Plasma and Ultrathin Foil, Phys. Rev. Lett. **122**, 014803 (2019).

[44] A. Pazzaglia, L. Fedeli, A. Formenti, A. Maffini, and M. Passoni, A theoretical model of laser-driven ion acceleration from near-critical double-layer targets, Comm. Phys. **3**, 133 (2020).

[45] A. Pukhov, Z.-M. Sheng, and J. Meyer-ter-Vehn, Particle acceleration in relativistic laser channels, Phys. Plasmas **6**, 2847 (1999).

[46] R. Lehe, C. Thaury, E. Guillaume, A. Lifschitz, and V. Malka, Laser-plasma lens for laser-wakefield accelerators, Phys. Rev. ST Accel. Beams **17**, 121301 (2014); D. F. Gordon, B. Hafizi, J. Palastro, Pushing particles in extreme fields, AIP Conf. Proc. **1812**, 050002 (2017); F. Li, K. Miller, X. Xu, F. Tsung, V. Decyk, W. An, R. Fonseca, W. Mori, A new field solver for modeling of relativistic particle-laser interactions using the particle-in-cell algorithm, Comput. Phys. Commun. **258**, 107580 (2021).

[47] A. V. Arefiev, G. E. Cochran, D. W. Schumacher, A. P. L. Robinson, and G. Chen, Temporal resolution criterion for correctly simulating relativistic electron motion in a high-intensity laser field, Phys. Plasmas **22**, 013103 (2015); Z. Gong, F. Mackenroth, T. Wang, X. Q. Yan, T. Toncian, and A. V. Arefiev, Direct laser acceleration of electrons assisted by strong laser-driven azimuthal plasma magnetic fields, Phys. Rev. E **102**, 013206 (2020).

[48] J. Wang, X. B. Li, L. F. Gan, Y. Xie, C. L. Zhong, C. T. Zhou, S. P. Zhu, X. T. He, and B. Qiao, Generation of Intense Vortex Gamma Rays via Spin-to-Orbital Conversion of Angular Momentum in Relativistic Laser-Plasma Interactions, Phys. Rev. Appl. **14**, 014094 (2020).

[49] A. Pukhov, Particle-In-Cell Codes for Plasma-based Particle Acceleration, CERN Yellow Rep. **1**, 181 (2016).

[50] L. P. Pugachev, N. E. Andreev, P. R. Levashov, and O. N. Rosmej, Acceleration of electrons under the action of petawatt-class laser pulses onto foam targets, Nucl. Instr. Meth. Phys. Res. A **829**, 88 (2016).

[51] A. Pukhov, X-dispersionless Maxwell solver for plasma-based particle acceleration, J. Comput. Phys. **418**, 109622 (2020).

[52] Y. Sentoku, K. Mima, S.-I. Kojima, and H. Ruhl, Magnetic instability by the relativistic laser pulses in overdense plasmas, Phys. Plasmas **7**, 689 (2000); P. H. Yoon and R. C. Davidson, Exact analytical model of the classical Weibel instability in a relativistic anisotropic plasma, Phys. Rev. A **35**, 2718 (1987).

[53] P. Sprangle, J. Krall, and E. Esarey, Hose-Modulation Instability of Laser Pulses in Plasmas, Phys. Rev. Lett. **73**, 3544 (1994).

[54] T. W. Huang, C. T. Zhou, H. Zhang, S. Z. Wu, B. Qiao, X. T. He, and S. C. Ruan, Relativistic laser hosing instability suppression and electron acceleration in a preformed plasma channel, Phys. Rev. E **95**, 043207 (2017).

[55] P. Gibbon, *Short Pulse Laser Interaction with Matter* (Imperial College Press, London, 2005).

[56] A. Macchi, M. Borghesi, and M. Passoni, Ion acceleration by superintense laser-plasma interaction, Rev. Mod. Phys. **85**, 751 (2013).

[57] X. F. Shen, B. Qiao, H. Zhang, S. Kar, C. T. Zhou, H. X. Chang, M. Borghesi, and X. T. He, Achieving Stable Radiation Pressure Acceleration of Heavy Ions via Successive Electron Replenishment from Ionization of a High-Z Material Coating, Phys. Rev. Lett. **118**, 204802 (2017).

[58] Z.-M. Sheng, K. Mima, Y. Sentoku, M. S. Jovanović, T. Taguchi, J. Zhang, and J. Meyer-ter-Vehn, Stochastic Heating and Acceleration of Electrons in Colliding Laser Fields in Plasma, Phys. Rev. Lett. **88**, 055004 (2002); Z.-M. Sheng, K. Mima, J. Zhang, and J. Meyer-ter-Vehn, Efficient acceleration of electrons with counterpropagating intense laser pulses in vacuum and underdense plasma, Phys. Rev. E **69**, 016407 (2004).

[59] H. Alfvén, On the motion of cosmic rays in interstellar space, Phys. Rev. **55**, 425 (1939).

[60] D. A. Brown *et al.*, ENDF/B-VIII. 0: The 8th major release of the nuclear reaction data library with CIELO-project cross sections, new standards and thermal scattering data, Nuclear Data Sheets **148**, 1 (2018).

[61] S. Kar *et al.*, Beamed neutron emission driven by laser accelerated light ions, New J. Phys. **18**, 053002 (2016).

[62] A. Curtis, C. Calvi, J. Tinsley, R. Hollinger, V. Kaymak, A. Pukhov, S. Wang, A. Rockwood, Y. Wang, V. N. Shlyaptsev, and J. J. Rocca, Micro-scale fusion in dense relativistic nanowire array plasmas, Nat. Commun. **9**, 1077 (2018).

[63] A. J. Kemp, S. C. Wilks, E. P. Hartouni, and G. Grim, Generating keV ion distributions for nuclear reactions at near solid-density using intense short-pulse lasers, Nat. Commun. **10**, 4156 (2019).

[64] X. R. Jiang, D. B. Zou, Z. J. Zhao, L. X. Hu, P. Han, J. Q. Yu, T. P. Yu, Y. Yin, and F. Q. Shao, Microstructure-Assisted Laser-Driven Photonuclear Pulsed Neutron Source, Phys. Rev. Appl. **15**, 034032 (2021).

[65] T. Nakamura, S. Kato, M. Tamimoto, and T. Kato, Stochastic acceleration by intense laser fields, Phys. Plasmas **9**, 1801 (2002).

[66] A. J. Lichtenberg and M. A. Lieberman, *Regular and Stochastic Motion* (Springer-Verlag, New York, 1984), Sec. 5.2.

[67] Y. Sentoku, K. Mima, P. Kaw, and K. Nishikawa, Anomalous Resistivity Resulting from MeV-Electron Transport in Overdense Plasma, Phys. Rev. Lett. **90**, 155001 (2003).

[68] J. Meyer-ter-Vehn and Z.-M. Sheng, On electron acceleration by intense laser pulses in the presence of a stochastic field, Phys. Plasmas **6**, 641 (1999).

[69] T. W. Huang, C. T. Zhou, A. P. L. Robinson, B. Qiao, H. Zhang, S. Z. Wu, H. B. Zhuo, P. A. Norreys, and X. T. He, Mitigating the relativistic laser beam filamentation via an elliptical beam profile, Phys. Rev. E **92**, 053106 (2015).

[70] A. B. Borisov, O. B. Shiryaev, A. McPherson, K. Boyer, and C. K. Rhodes, Stability analysis of relativistic and charge-displacement self-channelling of intense laser pulses in underdense plasmas, Plasma Phys. Control. Fusion **37**, 569 (1995).

[71] A. J. Kemp, F. Fiuza, A. Debayle, T. Johzaki, W. B. Mori, P. K. Patel, Y. Sentoku, and L. O. Silva, Laser plasma interactions for fast ignition, Nucl. Fusion **54**, 054002 (2014).

[72] L. C. Jarrott *et al.*, Visualizing fast electron energy transport into laser-compressed high-density fast-ignition targets, Nat. Phys. **12**, 499 (2016).

[73] M. M. Günther, O. N. Rosmej, P. Tavana, M. Gyrdymov, A. Skobliakov, A. Kantsyrev, S. Zähter, N. G. Borisenko, A. Pukhov, and N. E. Andreev, Forward-looking insights in laser-generated ultra-intense gamma-ray and neutron sources for nuclear application and science, Nat. Commun. **13**, 170 (2022).

[74] L. Willingale, G. M. Petrov, A. Maksimchuk, J. Davis, R. R. Freeman, A. S. Joglekar, T. Matsuoka, C. D. Murphy, V. M. Ovchinnikov, and A. G. R. Thomas, Comparison of bulk and pitcher-catcher targets for laser-driven neutron production, Phys. Plasmas **18**, 083106 (2011).

[75] B. Qiao, X. F. Shen, H. He, Y. Xie, H. Zhang, C. T. Zhou, S. P. Zhu, and X. T. He, Revisit on ion acceleration mechanisms in solid targets driven by intense laser pulses, Plasma Phys. Control. Fusion **61**, 014039 (2019).

[76] X. F. Shen, B. Qiao, A. Pukhov, S. Kar, S. P. Zhu, M. Borghesi, and X. T. He, Scaling laws for laser-driven ion acceleration from nanometer-scale ultrathin foils, Phys. Rev. E **104**, 025210 (2021).

[77] H. W. Koch and J. W. Motz, Bremsstrahlung cross-section formulas and related data, Rev. Mod. Phys. **31**, 920 (1959).

[78] R. Hollinger, C. Bargsten, V. N. Shlyaptsev, V. Kaymak, A. Pukhov, M. G. Capeluto, S. Wang, A. Rockwood, Y. Wang, A. Townsend, A. Prieto, P. Stockton, A. Curtis, and J. J. Rocca, Efficient picosecond x-ray pulse generation from plasmas in the radiation dominated regime, Optica **4**, 1344 (2017).

[79] F. Albert and A. G. R. Thomas, Applications of laser wakefield accelerator-based light sources, Plasma Phys. Control. Fusion **58**, 103001 (2016).

[80] M. Borghesi, A. Schiavi, D. H. Campbell, M. G. Haines, O. Willi, A. J. MacKinnon, L. A. Gizzi, M. Galimberti, R. J. Clarke, and H. Ruhl, Proton Imaging: A Diagnostic for Inertial Confinement Fusion/Fast Ignitor Studies, Plasma Phys. Control. Fusion **43**, A267 (2001).

[81] www.gauss-centre.eu.